Purdue University
Purdue e-Pubs

CTRC Research Publications | Cooling Technologies Research Center

2012

Modeling and Design Optimization of Ultra-Thin Vapor Chambers for High Heat Flux Applications

R. Ranjan
United Technologies Research Center

J. Y. Murthy
Purdue University

S V. Garimella
Purdue University, sureshg@purdue.edu

D. H. Altman
Raytheon Integrated Defense Systems

M. T. North
Thermacore, Inc.

Follow this and additional works at: http://docs.lib.purdue.edu/coolingpubs

Ranjan, R.; Murthy, J. Y.; Garimella, S V.; Altman, D. H.; and North, M. T., "Modeling and Design Optimization of Ultra-Thin Vapor Chambers for High Heat Flux Applications" (2012). *CTRC Research Publications.* Paper 186.
http://dx.doi.org/10.1109/TCPMT.2012.2194738

This document has been made available through Purdue e-Pubs, a service of the Purdue University Libraries. Please contact epubs@purdue.edu for additional information.

Modeling and Design Optimization of Ultra-Thin Vapor Chambers for High Heat Flux Applications

Ram Ranjan, Jayathi Y. Murthy, Suresh V. Garimella, David H. Altman, and Mark T. North

Abstract—**Passive phase-change thermal spreaders such as vapor chambers have been widely employed to spread the heat from small-scale high-flux heat sources to larger areas. In the present work, a numerical model for ultra-thin vapor chambers has been developed which is suitable for reliable prediction of the operation at high heat fluxes and small scales. The effects of boiling in the wick structure on the thermal performance are modeled and the model predictions are compared with experiments on custom-fabricated vapor chamber devices. The working fluid for the vapor chamber is water and a condenser side temperature range of 293 K to 333 K is considered. The model predictions agree reasonably well with experimental measurements and reveal the input parameters to which thermal resistance and vapor chamber capillary limit are most sensitive. The vapor space in the ultra-thin devices offers significant thermal and flow resistances when the vapor core thickness is in the range of 0.2-0.4 mm. The performance of a 1 mm thick vapor chamber is optimized by studying the variation of thermal resistance and total flow pressure drop as functions of the wick and vapor core thicknesses. The wick thickness is varied from 0.05 to 0.25 mm. Based on the minimization of a performance cost function comprising the device thermal resistance and flow pressure drop, it is concluded that the thinnest wick structures (0.05 mm) are optimal for applications with heat fluxes below 50 W/cm^2, while a moderate wick thickness of 0.1 mm performs best at higher heat flux inputs (> 50 W/cm^2).**

Index Terms—**Vapor chamber, heat spreader, heat pipe model, thermal ground plane, electronics cooling, boiling**

NOMENCLATURE

A	area (m^2).
C_E	Ergun's coefficient, 0.55.

Manuscript received August 2, 2011, and in revised form February 20,2012. This material is based upon work supported by the Defense Advanced Research Projects Agency (DARPA) and Space and Naval Warfare Systems Center (SPAWAR/SYSCEN) San Diego, CA under Contract No. N66001-08-C-2011.

R. Ranjan is with United Technologies Research Center, East Hartford CT 06108 USA.

J. Y. Murthy, and S. V. Garimella are with the School of Mechanical Engineering and Birck Nanotechnology Center, Purdue University, West Lafayette, IN 47907 USA (Corresponding author e-mail: sureshg@purdue.edu).

D. H. Altman is with Raytheon Integrated Defense Systems, Sudbury, MA 01776 USA.

M. T. North is with Thermacore, Inc., 780 Eden Rd, Lancaster, PA 17601 USA.

CF	optimization cost function
CTE	coefficient of thermal expansion, K^{-1}.
g	acceleration due to gravity, m/s^2.
h_{evap}	convection heat transfer coefficient defined for evaporation, W/m^2K.
h_{fg}	latent heat, J/kg .
k	thermal conductivity, W/m K.
k_{eff}	effective thermal conductivity, W/m K.
K	permeability of the porous medium, m^2.
L	length, m.
$\dot{m}''$	mass flux, kg/m^2s.
M	mass, kg.
$\bar{M}$	molecular weight, g/mol.
P	pressure, Pa.
$\dot{q}''$	heat flux, W/m^2.
R	thermal resistance, K/W.
$\bar{R}$	universal gas constant, J/molK .
r	radius, m.
t	time, s.
T	temperature, K.
TGP	thermal ground plane.
u	x-direction velocity, m/s.
v	y-direction velocity, m/s.
$\vec{V}$	velocity vector, m/s .
w	z-direction velocity, m/s.
w_1, w_2	weights assigned for performance optimization.
x	axial coordinate; axial distance, m.
y, z	transverse direction coordinates; transverse distance, m.

Greek symbols

α	thermal diffusivity, m^2/s.

γ_{lv} surface tension between liquid and vapor phases, N/m.

Ω area on the upper surface of the vapor chamber.

$\hat{\sigma}$ accommodation coefficient.

ρ density of liquid, kg/m^3.

ε porosity of the wick.

θ contact angle between liquid and solid surface.

v kinematic viscosity, m^2/s.

μ dynamic viscosity, Ns/m^2.

Subscripts

a adiabatic section.

c condenser.

e evaporator.

equ equilibrium.

eff effective.

i, *lv* interface.

l liquid.

max maximum.

norm normalized.

op operating pressure.

ref reference.

s solid.

sat saturation condition.

v vapor.

w wall.

I. INTRODUCTION

Two-phase cooling devices such as heat pipes and vapor chambers have proven to be among the most efficient passive cooling devices for electronics cooling. Flat heat pipes and vapor chambers [1-5] are widely used as high-conductivity heat spreaders in various kinds of electronic systems. The continuously increasing power density of modern electronics demands novel thermal spreaders with higher thermal conductivity and high heat transport capability. Also, high-power electronics can

benefit from improved CTE-matching, which enables the use of high performance die attach materials, such as solder. Generally, the maximum heat transport capability and thermal conductivity of such devices are governed by the wick structure of the device. However, the vapor space may pose a significant thermal resistance at small length scales. In recent work, the authors [6,7] studied the wicking and evaporation characteristics of various microstructures to be used in heat pipes and concluded that sintered particle wicks have the best performance characteristics among those considered. Numerical models for vapor chambers which account for the effects of thin-film evaporation and Marangoni convection during the change of phase of the working fluid in the wick structure have also been developed [8,9]. These models have led to a better understanding of the mechanisms of heat transport in the two-phase cooling devices. Also, the optimization of the device geometry under a given set of manufacturing constraints has become possible due to the development of these numerical models.

Vadakkan *et al.* [10,11] developed a three-dimensional numerical model to study the performance of flat heat pipes with multiple discrete heat sources. In a recent study, Do *et al.* [12] presented a mathematical model for predicting the thermal performance of a flat micro heat pipe with a rectangular-grooved wick structure. They considered the effects of liquid-vapor interfacial shear stress and contact angle on device performance. Carbajal *et al.* [13] used a quasi-3D numerical analysis to obtain the temperature distribution on the back side of a flat heat pipe. They demonstrated that the flat heat pipe led to a more uniform temperature distribution on the condenser side compared to a solid heat spreader. Koito *et al.* [14] developed a numerical model to solve the flow and energy equations in vapor chambers and estimated the capillary pressure head necessary to circulate the working fluid inside the vapor chamber. Simplified resistance network models [15] for heat pipes have also been developed, and assume a given heat transfer coefficient for the evaporator section of the heat pipe. Such models also consider the resistance of the vapor core to be negligible which may not be accurate at small length scales and for very thin vapor chambers.

The numerical models for heat pipes developed in the literature as discussed above are not applicable to higher heat flux conditions under which nucleate boiling occurs in the wick structure. At high heat flux inputs, Weibel *et al.* [16] showed that nucleate boiling occurs in the wick structure of a heat pipe, leading to a reduction in the wick thermal resistance. In the present work, a numerical model is developed for prediction of the thermal performance of very thin vapor chambers, also known as a thermal ground plane (TGP), at high heat flux inputs. The model considers the effects of boiling in the wick structure on the thermal performance of the device. Heat transfer experiments have been conducted on custom-fabricated TGPs to validate the numerical model at various heat inputs. Results from this study reveal the effects of device scaling on its performance. The study of different TGPs of different geometric dimensions leads to a determination of the factors to which the TGP thermal performance is most sensitive. The simulations performed on a 1 mm thick TGP, with a 0.2 mm thick vapor core, suggest that the flow and thermal resistances offered by the vapor core are significant in comparison to the wick and substrate wall

resistances. The design optimization of such a thin vapor chamber device is performed by varying the geometrical design parameters, *viz.*, wick and vapor core thicknesses, while keeping the substrate wall thickness fixed.

II. PROBLEM DESCRIPTION

The geometry of the device under consideration, as well as the material properties of the various components of the device, are described here.

A. Device Geometry

The cross-sectional and plan views of the TGP vapor chamber considered are shown in Fig. 1. The device has a foot-print area of 30 mm × 30 mm and a thickness of 3 mm. The heat input is applied on a 5 mm × 5 mm area (evaporator) on the upper surface of the device while the lower surface (condenser) is subjected to cooling conditions. The shell of the TGP device is made of 0.51 mm thick copper-molybdenum-copper (CuMoCu) and contains a 1 mm thick sintered wick structure on the inside of the heated side. Four circular porous posts of 2 mm diameter each, with solid copper cores of 1 mm diameter, are included to provide mechanical integrity to the ultra-thin vapor chamber during operation at sub-atmospheric internal pressures. The posts are fabricated symmetrically about the center of the device with their centers lying on the four corners of a 10.16 mm square. Two designs – one with a 200 µm thick wick and the other with no wick on the condenser side – are fabricated. The second design allows a quantification of the effect of a wick-less condenser side on device performance. The experiments for this study, described in Altman *et al.* [17], show that the two alternate designs do not lead to any significant change in the thermal performance of the vapor chamber at low heat flux inputs (< 100 W/cm^2). Only the first design with a 200 µm thick wick on the condenser side is considered in the modeling effort here. For higher heat inputs, a semi-empirical approach is employed to predict the TGP performance. The predictions from the model are compared with the experimental results for both vapor chamber designs of the vapor chamber. In the case of the wick-less condenser, a thin liquid film would form on the inside wall due to condensation of vapor. This liquid film does not materially affect the thermal performance of the device, as noted from the experiments. In section 4, it will be shown that the 200 µm thick wick on the condenser side poses an insignificant resistance in comparison to the total thermal resistance of the device; good agreement is found between model predictions and experimental results from both vapor chamber designs.

B. Material Properties

The wall of the vapor chamber is made of a copper-molybdenum-copper layered structure (13% Cu, 74% Mo and 13% Cu). The composition of the walls was determined to provide an acceptable CTE-match to enable high performance thermal interface material (TIM) attach for the devices of interest. The thermal conductivity, specific heat and density of this composite layer are

computed from an equivalent thermal resistance of Cu (13%), Mo (74%) and Cu (13%) layers in series. The working fluid is water, while the wick structure is made of sintered particles of 100 μm average diameter. The wick structure with a porosity of 50% has a capillary radius (r_c) of 23.5 μm and a permeability of 9.47×10^{-12} m^2. The material properties used in the model are presented in Table I.

III. NUMERICAL METHODOLOGY

The numerical model employed here is adapted from previous work by the authors [8,10,11]. An equilibrium model for heat transfer accounts for the transient variations in the rates of evaporation and condensation at the liquid-vapor interface in the device and the resulting pressurization of the vapor core. A Brinkman-Forchheimer extended Darcy model is employed for fluid flow in the wick. The transient change in vapor density due to pressurization upon heating is calculated using the ideal gas state equation. The vapor flow is assumed to be laminar and incompressible. The phase-change mass flow rate due to evaporation/ condensation and the temperature and pressure at the liquid-vapor interface are determined using an energy balance at the interface in conjunction with kinetic theory and the Clausius-Clapeyron equation. The energy balance at the interface includes convection and conduction on the liquid and vapor sides. The vapor flow and the temperature and hydrodynamic pressure fields are computed from coupled continuity, momentum and energy equations in the vapor and wick regions, and a conduction analysis in the wall. The model assumes that the wick is saturated with liquid throughout, which is required to prevent dryout.

To accommodate transient changes in the vapor and liquid mass under the assumption of a liquid-saturated wick, the volume-averaged density of the liquid is modified based on the mass balance. The model assumes all thermophysical properties to be constant except for the vapor density, which is found from the operating pressure P_{op} and the local temperature using the perfect gas law.

A. Governing Equations and Boundary Conditions

Under the assumptions discussed above, the generalized governing equations for the wick and vapor regions may be written as shown below. The continuity equation for the wick and the vapor core is

$$\varepsilon \frac{\partial \rho}{\partial t} + \nabla.(\rho \vec{V}) = 0 \quad (1)$$

The term $\frac{\partial \rho}{\partial t}$ accounts for mass addition or depletion in the vapor and liquid spaces. The three-dimensional momentum equations in the wick and the vapor core are

$$\frac{\partial \rho u}{\partial t} + \nabla.(\rho \vec{V} u) = -\frac{\partial \varepsilon p}{\partial x} + \nabla.(\mu \nabla u) - \frac{\mu \varepsilon}{K} u - \frac{C_E \varepsilon}{K^{\frac{1}{2}}} \rho |\vec{V}| u \quad (2)$$

$$\frac{\partial \rho v}{\partial t} + \nabla.(\rho \vec{V} v) = -\frac{\partial \varepsilon p}{\partial y} + \nabla.(\mu \nabla v) - \frac{\mu \varepsilon}{K} v - \frac{C_E \varepsilon}{K^{\frac{1}{2}}} \rho |\vec{V}| v \quad (3)$$

$$\frac{\partial \rho w}{\partial t} + \nabla.(\rho \vec{V} w) = -\frac{\partial \varepsilon p}{\partial z} + \nabla.(\mu \nabla w) - \frac{\mu \varepsilon}{K} w - \frac{C_E \varepsilon}{K^{\frac{1}{2}}} \rho |\vec{V}| w \quad (4)$$

In the vapor core, permeability $K = \infty$ and porosity $\varepsilon = 1$. The energy equation in the wall, wick and vapor core is

$$\frac{\partial (\rho C)_m T}{\partial t} + \nabla.[(\rho C)_l \vec{V} T_l) = \nabla.(k_{eff} \nabla T) \quad (5)$$

Here $(\rho C)_m$ assumes different values in the wall, wick and vapor core:

Wall: $(\rho C)_m = (\rho C)_s$

Wick: $(\rho C)_m = (1-\varepsilon)(\rho C)_s + \varepsilon (\rho C)_l$ (6)

Vapor core: $(\rho C)_m = (\rho C)_v$

Also, k_{eff} and ρ are the effective conductivity and density in the region of interest and assume appropriate values in the wall, wick and vapor core. In the wick (composed of sintered copper particles), an effective conductivity value of 40 W/mK is assumed [18].

The following boundary conditions are imposed on the domain.

1. Wick-vapor interface: Change of phase from liquid to vapor is assumed to occur at the wick-vapor core interface. The interface temperature T_i is obtained from the following energy balance at the interface

$$-k_{wick} A_i \frac{\partial T}{\partial y} + m_i C_l T_i = -k_v A_i \frac{\partial T}{\partial y} + m_i C_v T_i + m_i h_{fg} \quad (7)$$

Here, $m_i < 0$ denotes evaporation and $m_i > 0$ denotes condensation. The interface pressure P_i is obtained from the Clausius-Clapeyron equation, with P_0 and T_0 being reference values:

$$\frac{R}{h_{fg}} \ln\left(\frac{P_i}{P_o}\right) = \frac{1}{T_o} - \frac{1}{T_i} \quad (8)$$

The interface mass flux is calculated using kinetic theory of gases [19]:

$$\left(\frac{2\hat{\sigma}}{2-\hat{\sigma}}\right)\left(\frac{\bar{M}}{2\pi\bar{R}}\right)^{1/2}\left(\frac{P_v}{(T_v)^{1/2}} - \frac{P_i}{(T_i)^{1/2}}\right) = \dot{m}_i'' \quad (9)$$

The above expression has been obtained with the assumption that the mean evaporation coefficient is equal to the mean condensation coefficient, where their variation with temperature and pressure may be assumed to be small. A value of unity for the accommodation coefficient has been used in the present work [20,21]. The evaporated and condensed mass is assumed to flow normal to the interface when accounting for transport due to evaporation/ condensation.

2. Wick-wall interface:

$$u = 0,\ v = 0, w = 0 \tag{10}$$

3. Upper wall:

Evaporator section:

$$k_w \frac{\partial T}{\partial z} = q_e \quad \Omega_e : -L_e \le x \le L_e, -L_e \le y \le L_e \tag{11}$$

Adiabatic wall:

$$\begin{gathered} \frac{\partial T}{\partial z} = 0 \text{ on } \Omega - \Omega_e, \\ \Omega : -L_{TGP}/2 \le x \le L_{TGP}/2, -L_{TGP}/2 \le y \le L_{TGP}/2 \end{gathered} \tag{12}$$

4. Lateral walls:

$$\text{Adiabatic walls: } \frac{\partial T}{\partial n} = 0 \tag{13}$$

5. Bottom wall:

Condenser section:

$$\begin{gathered} -k_w \frac{\partial T}{\partial z} = h_c (T - T_c) \text{ on} \\ -L_{TGP}/2 \le x \le L_{TGP}/2, -L_{TGP}/2 \le y \le L_{TGP}/2 \end{gathered} \tag{14}$$

where, h_c is the convective heat transfer coefficient at the outer surface of the condenser section. Its value (8240 W/m^{2}K) in the present work is decided based on the experimental setup. In addition, the following initial conditions are imposed:

$$T(x, y, z, 0) = T_i \qquad P_{op}(t = 0) = P_{sat}(T_i) \tag{15}$$

Additional details of the numerical method are available in [8,10,11]. The transient governing equations are solved using the commercial CFD solver FLUENT [22]. Suitable user-defined functions (UDFs) are developed to compute the evaporation/condensation mass flow rates, temperature and pressure at the wick-vapor interface, as well as the liquid and vapor densities at every time step. The attainment of steady state is identified in this work as the time at which the heat transfer rate on the condenser side reaches within 2% of the value at the evaporator.

B. Evaporation versus Boiling Regimes

Evaporation and condensation at the wick-vapor interface are the primary mechanisms for phase change of the working fluid in a heat pipe. As the heat input to a vapor chamber is increased, the operating temperature and pressure increase. At a certain input heat flux, incipience of nucleate boiling occurs in the wick structure of the device. Boiling incipience leads to a higher heat transfer coefficient at the wall-wick interface, and thus, leads to a decrease in the thermal resistance of the device. Weibel *et al*.

[16] reported the incipient heat flux to be in the range of 50 W/cm^2 for 200 µm thick sintered particle wicks using visualization experiments. They tested the wick structures for their thermal performance with water as the working fluid in an experimental facility under conditions similar to those in a vapor chamber. The experiments were performed on wicks of varying thickness and pore size with a heat input area of 5 mm × 5 mm and in a saturated vapor environment. The thermal resistance of the wick structure was shown to decrease upon the incipience of boiling, and the extent of the decrease was found to be equivalent to a removal of the resistance of the wick structure in the series resistance network. Based on these quantitative measurements and visualizations, Weibel *et al.* showed that while evaporation at the lower heat fluxes occurs at the liquid layer at the surface of the wick (the wick-vapor core interface), the location of phase change upon the incipience of boiling at higher fluxes transfers to the wall-wick interface at the base of the wick instead.

In the present work, a semi-empirical approach is adopted to predict the performance of the vapor chamber device under boiling conditions at high heat flux inputs. The incipient heat flux is chosen based on the experiments performed on the custom fabricated vapor chambers and the incipient temperature for nucleate boiling is determined in the model based on the incipient heat flux. Nucleate boiling is assumed to start at the wick-wall interface and the spatial extent in the wick over which boiling occurs is determined by the local wick temperature. In order to predict the thermal performance of the device with boiling at the base of the wick structure, the thermal resistance of the portion of the wick undergoing boiling is minimized. This is done by increasing the thermal conductivity of the wick region undergoing boiling. For the given incipient heat flux, the boiling wick thermal conductivity, k_{wick_boil}, is adjusted so that the TGP thermal resistance predicted by the numerical model agrees with the experimental value. The same value for k_{wick_boil} is used for higher heat flux inputs. In this study, k_{wick_boil} has been taken as 175.3 W/m K and leads to a reasonable match between the model predictions and experimental results. It should be noted that the boiling wick thermal conductivity, k_{wick_boil}, is a semi-empirical quantity. This is in contrast to the quantity k_{eff} (in eq. (5)) which represents the wick bulk thermal conductivity obtained as $k_{eff} = \varepsilon * k_l + (1- \varepsilon) * k_s$. When boiling occurs in the wick, the semi-empirical k_{wick_boil} replaces k_{eff} for predicting the device performance under boiling conditions.

IV. EXPERIMENTAL SETUP

A schematic diagram of the experimental test setup is shown in Fig. 2. The heat input to the TGP device is applied through a copper heater block capable of generating inputs as high as 800 W/cm^2. The lower temperature boundary condition is prescribed at the bottom surface of the vapor chamber via contact with a cooling water jacket, and is measured via a thermocouple block made of copper as shown. Fifteen thermocouples are placed at various locations in the experimental facility, as shown in Fig. 2, in order to map the local temperature. Heat flow through the copper heater block is determined using linear regression analysis from three in-line type-T immersion probe-style thermocouples inserted into the copper block. The temperature of the top

surface of the vapor chamber under test is sensed by a custom thermocouple made from special limit of error (SLE) thermocouple wire that is insulated from the Cu block with a small ceramic tube and makes physical (and electrical) contact with the Cu surface through a thin-layer of Shin-etsu X23-7762 thermal grease. The heat input to the TGP device is calculated based on the temperature measurements in the copper heater block. It should be noted that this is not a conservative estimate of the heat input to the device since heat losses through radiation and natural convection occur from various parts of the test facility. Shin-etsu grease is used to minimize interface resistance between the heater block at the TGP, while sheets of a thermal interface material from Bergquist Company are used to interface the lower thermocouple block with the TGP and the cooling jacket. Additional details of the experimental setup are available in Altman *et al.* [17].

Fig. 3 shows the blocks representing various parts of the test setup in the model. These include the TGP vapor chamber device, the thermocouple block and the two thermal contact pads between the TGP and thermocouple (TC) block and between the TC block and the cooling water jacket. Input heat flux is applied on the evaporator surface of the TGP while a convective boundary condition, representing the effect of cooling water jacket (h_c = 8240 W/m^{2}K), is applied on the bottom surface of the lower thermal interface pad. The water temperature in the cooling jacket is kept constant in the experiments and the heat flux is varied at the evaporator. The thermal interface pads are modeled as a 0.05 mm thick planar material with a thermal conductivity of 0.5 W/m K.

A 1-D thermal resistance network model for the test setup is shown in Fig. 2. Temperature T_1 is measured at the heater block while T_2 represents the evaporator temperature. T_3 - T_{14} are measurements from the thermocouples distributed symmetrically in the thermocouple block. The input heat flux is increased stepwise and steady-state temperatures are measured at various thermocouple locations. Resistances R_1 - R_4, denoting different components of the test setup as shown in Fig. 2, are obtained from the measured temperatures. R_4 represents the thermal resistance from TGP evaporator to the coolant (T_2 to T_{15}) and has been referred as the stack resistance in latter sections.

V. RESULTS & DISCUSSION

Results from the numerical model developed in this work are first validated against the two TGP devices described in section II.A. The model validation is followed by a discussion of the flow and temperature fields inside the device for a given heat flux. Finally, the numerical model is used to identify some of the geometrical parameters to which the device performance is most sensitive.

A. Model Validation

Fig. 4(a) shows the various parts of the computational domain. The model includes the TGP device, thermal interface material between the TGP and the TC block, TC block made of copper, and the thermal interface material between the TC block and the cooling water jacket. Only a quarter of the assembly is included in the model, exploiting existing symmetries. Thermophysical properties of the thermal interface material (TIM) and the thermocouple block along with the boundary conditions for the model are presented in Table II. The simulations are performed with a 200 µm thick wick structure on the condenser side of the TGP.

The wick and vapor domains of the TGP are shown in Fig. 4(b). The wick is modeled as a continuous domain with a thickness of 1 mm on the evaporator side and 200 µm on the condenser side of the vapor chamber. The wicks on the condenser and evaporator sides are modeled as a connected domain via a 200 µm thick wick along the side walls. Also, the wicks on the two sides are integrated with that around the circular porous posts.

A simplified 1-D resistance network model for the TGP device is shown in Fig. 5(a) and is used to obtain first-order estimates of various resistances in the vapor chamber. The various resistances represent: (a) the spreading in the substrate (CuMoCu) and wick on the evaporator side (R_{TGP1}), (b) conduction in the substrate and wick (R_{TGP2}), (c) evaporation at the liquid-vapor interface on the evaporator side (R_{TGP3}), (d) the vapor core (R_{TGP4}), (e) condensation at the liquid-vapor interface on the condenser side (R_{TGP5}), (f) conduction in the wick on the condenser side (R_{TGP6}), and (g) conduction in the substrate wall on the condenser side (R_{TGP7}). R_{TGP1} is computed from a numerical model where the heat conduction equation is solved in the substrate wall (0.51 mm thickness) and the wick (1 mm thickness). The input heat flux is applied on the evaporator surface and the wick-vapor interface (lower boundary of the domain) is subjected to a convection boundary condition with a vapor temperature 298 K and convective heat transfer coefficient = 10^6 W/m^{2}K. This coefficient signifies the high cooling heat transfer rate [7] due to evaporation. Fig. 5(b) shows the temperature contours in the substrate and wick, obtained from the model for computation of the spreading resistance with k_{wick} = 40 W/mK. The other resistances (R_{TGP2}-R_{TGP7}) are calculated based on the given properties, *viz.*, the thickness and thermal conductivities of various parts. The evaporative and condensation resistances of the liquid-vapor interfaces are computed based on a heat transfer coefficient of 10^6 W/m^{2}K.

The values obtained for various resistances in the 1-D network model (Fig. 5(a)) of the TGP, as presented in Table III, are based on the material properties and geometry described in Table I and Fig. 1, respectively. The thermal resistance of the vapor core is assumed to be negligible (R_{TGP4} ~ 0) [15] as is common practice in the literature. From the values for resistances, it can be observed that R_{TGP1} poses the highest resistance in the TGP. Also, the resistance offered by the wick on the condenser side, R_{TGP6}, is negligible in comparison to the total resistance of the TGP. This is consistent with the observed independence of the experimental results on the presence of a wick on the condenser side for the range of lower heat flux inputs (< 100 W/cm^2). It

will also be shown below that the experimentally measured thermal resistance of the TGP with a wick-less condenser agrees well with the model predictions for the TGP with a 200 μm thick wick on the condenser side.

TGP with condenser wick

Fig. 6 presents a comparison between the model predictions for the stack resistance R_4 with the experimental measurements. Experiments were performed on the fabricated TGP device, denoted as TGP 1. The bars on the experimental data reflect the uncertainties in the temperature measurement. The thermal conductivity of the wick in the fabricated TGPs is unknown and is varied in the range 30-40 W/mK. In Fig. 6, the model predictions are shown for k_{wick} = 30 and 40 W/mK. For the higher wick thermal conductivity (40 W/mK), the model predictions for thermal resistance are lower than the experimental values. Based on this comparison, a wick thermal conductivity of 30 W/mK seems suitable for the sintered particle wick structures fabricated in the present work. The comparison presented in Fig. 6 shows that the model predictions are in reasonable agreement with the experimental values. Also, the thermal resistance of the TGP is shown to be relatively constant over input heat fluxes ranging from 18 to 220 W/cm^2; this implies that boiling incipience did not occur in the vapor chamber over these input heat fluxes. The thermal resistance of all other TGP designs is shown in the next section to decrease with increasing heat flux, typically at a heat flux input of ~110 W/cm^2. This appears to indicate that the incipience of boiling is delayed in TGP 1 due to the presence of the wick structure on the condenser side. A detailed study of the impact of the wick structure on the condenser side is needed to fully understand this delayed boiling incipience.

TGP with no condenser wick

In a vapor chamber, the absence of a wick structure on the condenser side may lead to a decrease in the thermal resistance of the device. In this case, the vapor condenses on the inner wall of the device, leading to the formation of a thin condensate liquid film. The condensate forms a continuous liquid film on the wick-less internal wall of the vapor chamber and the liquid is conveyed back to the evaporator section by capillary action of the wick structure on the side walls and porous posts. Such TGPs with no wick on the condenser side were also fabricated in order to experimentally compare their performance with TGPs that do feature a condenser wick. As discussed earlier, the thermal resistance of the TGP vapor chambers of the two designs performed similarly in the experiments for low heat flux inputs (< 100 W/cm^2); thus the model for the device with a 200 μm thick wick structure on the condenser side was also used to predict the performance of the TGPs with no condenser wick. The TGP performance in the higher heat flux input regime was predicted by using a semi-empirical approach, as described in section III.B.

Fig. 7 shows a comparison between the model predictions and the experimental values for the stack resistance R_4 (Fig. 2) as a function of the input heat flux. The numerical model considers two values of the wick thermal conductivity, 30 and 40 W/mK. The experimental values of the stack resistance are obtained from two sets of experiments each performed on two nominally identical TGP vapor chambers (TGP 2 and TGP 3). From the experimental values, R_4 is observed to be nearly constant in the

lower heat flux regime (< 110 W/cm^2), while it decreases in the range ~110 to 185 W/cm^2. While both the devices perform similarly at large heat fluxes, large scatter in the data is observed at low heat inputs. This scatter in the experimental data is primarily attributed to manufacturing and experimental uncertainties [17]. Complex thermal and hydrodynamic phenomena occurring in the vapor chamber may also contribute to some of the observed variations, but are not understood to an extent that allows their inclusion in the modeling effort. For higher input heat fluxes (> 185 W/cm^2), R_4 attains a near-constant value (~0.7 K/W). This variation suggests that the incipience of boiling occurs in the vapor chamber for an input heat flux of ~110 W/cm^2. This heat flux is chosen in the numerical model as the incipient heat flux for nucleate boiling in the wick structure, and the highest temperature at the wick-wall interface is computed for this incipient heat flux. Based on this simulation, the incipience temperature for nucleate boiling in the wick structure is determined to be 320 K. This incipient temperature for boiling is used in all other simulations reported here. This is the only criterion prescribed in the numerical model for the onset of nucleate boiling in the wick structure.

The region undergoing boiling in the wick structure is then determined based on the incipient temperature distribution at the wick-wall interface and the thermal conductivity of this portion of the wick is set at a higher value (k_{wick_boil} = 175.3 W/mK) to match the value of R_4 obtained from the experiments at the incipient heat flux. The same incipience temperature and k_{wick_boil} are used in the numerical model to predict the performance at all higher heat fluxes. The heat flux range of 0-110 W/cm^2 is identified as the pure evaporation regime where evaporation and condensation are the only phase change mechanisms in the TGP. Over the heat flux range of 110-185 W/cm^2, transition to boiling occurs and boiling spreads to the whole wick on the heated side at input heat fluxes of 185 W/cm^2 or greater. In the transitional boiling range of heat flux, the resistance of the TGP decreases as the area experiencing boiling in the wick region increases, since this part of the wick poses much lower resistance to heat transfer. For higher heat fluxes (> 185 W/cm^2), the TGP resistance becomes constant since there is no further increase in the area of the wick undergoing boiling. The model predictions are in reasonable agreement with the experimental results and the model is seen to capture the three operating regimes of the TGP vapor chamber. For the higher wick thermal conductivity (k_{wick} = 40 W/mK), boiling incipience occurs at a higher heat flux relative to the case with k_{wick} = 30 W/mK. In the transition and pure boiling regimes, both values of the wick thermal conductivity lead to similar performance predictions as would be expected. In the pure boiling regime, the wick thermal conductivity is set to k_{wick_boil} and R_4 is independent of the choice of k_{wick}. In the remaining simulations in this work, k_{wick} is set as 30 W/mK due to the somewhat better match with experiments in the evaporation regime.

Fig. 7 also compares the performance of the TGP device with a solid heat spreader (3 mm thick) made of the wall material (CuMoCu, k = 167.8 W/mK). *It can be seen that the use of a vapor chamber as a heat spreader is only justified for higher heat fluxes (> 100 W/cm^2) for the given geometry and the mounting surface temperature.* Similar constraints on the benefits of using

a vapor chamber in electronics cooling have been discussed in Sauciuc *et al.* [2]. However, the drop in the resistance occurs at a lower heat flux when the mounting surface temperature is raised, thus making the TGP a more effective heat spreader at lower heat fluxes.

B. Flow and Temperature Fields

The flow and temperature fields in the TGP device for an input heat flux of 89 W/cm^2 and a wick thermal conductivity of 30 W/mK are presented here. The TGP with a wick on the condenser side (200 μm thick) is considered. The steady-state temperature contours on the external boundaries of the computational domain are shown in Fig. 8. It is noted that the steepest temperature gradients are observed in the substrate wall (in the lateral direction) and in the wall and the wick structure (in the transverse direction), both on the evaporator side. This signifies that the limiting resistances in the performance of the device are offered by the substrate wall and the wick.

Fig. 9(a), (b) and (c) present the velocity vectors on various vertical planes in the wick structure, on a horizontal plane in the wick structure and on a horizontal plane in the vapor core. It is interesting to observe that the condensate in the condenser wick structure returns to the evaporator side through two different paths, the wick structure on the side walls and the porous posts, as shown in Fig. 9(a). The presence of the porous posts offers a shorter path for liquid return to the evaporator area, thus decreasing the total liquid pressure drop. Thus, the porous posts lead to an increase in the capillary limit and the maximum heat transport capability of the vapor chamber. Fig. 9(b) shows the liquid flow in the wick structure on the evaporator side of the device while Fig. 9(c) shows the flow of vapor from the center of the device towards its side walls.

The temperature on the external surfaces (evaporator, adiabatic and condenser) of the vapor chamber is shown in Fig. 10(a). The temperature is highest at the center of the device on the evaporator side and drops in the adiabatic region. The lower surface of the device, *i.e.* the condenser wall, has a uniform temperature. This shows that the vapor chamber works as an excellent heat spreader. Fig. 10(b) shows the heat flux on the condenser (bottom boundary) surface of the TGP. It can be observed that the heat flux output from the bottom surface of the TGP (condenser surface) is quite uniform, again depicting the heat spreading of the device.

The variations of the steady-state flow pressure drops in the wick and vapor core of the device are presented as a function of the input heat flux in Fig. 11. The vapor pressure drop is observed to be very small in comparison to the liquid pressure drop in the device at any input heat flux. It accounts for approximately 10% of the total pressure drop for a heat flux range of 18-89 W/cm^2. The variations of pressure drops are observed to be linearly proportional to the input heat flux. The total pressure drop from these predictions follows the relationship:

$$\Delta P_{total} = 3.89\dot{q}'' \tag{16}$$

The available capillary pressure for the liquid transport in the device can be calculated based on the pore radius of the sintered particle wick structure [6]. For a sintered particle wick structure with an average particle diameter of 100 μm, the maximum non-dimensional capillary pressure ($\Delta P_{cap} r / \gamma_{lv}$) is 5.21. Based on eq. (16), the capillary limit of the TGP device would be ~1929 W/cm^2. It should be noted that this limit corresponds to a single phase pressure drop in the device; with the incipience of boiling, the liquid pressure drop may be significantly higher than that predicted by the present model, and may reduce the capillary limit significantly. It may be noted that even at fluxes as high as 500 W/cm^2, dry-out of the vapor chamber has not been noted in the experiments [16,17].

C. Performance of an Ultra-Thin Device

Using the model developed above, the geometry of an ultra-thin TGP vapor chamber (total thickness of 1 mm) is optimized here. Such thin devices are of importance for the thermal management of thickness-constrained, high heat flux microelectronics packages. It will be shown in this section that the device performance does not scale linearly with its size, and that small length scale effects become important for thinner devices. The device performance is also strongly correlated to the ambient temperature on the condenser side. The numerical model developed in this study resolves the effects of scaling which is essential in the design of such devices.

The performance of a 1 mm thick TGP with 0.25 mm thick substrate wall, 0.2 mm thick wick on the evaporator side and 0.05 mm thick wick on the condenser side, and a 0.25 mm thick vapor core (referred to as the 'nominal' TGP in the rest of this discussion) is first simulated and presented. The wick thermal conductivity, permeability and porosity are taken as 30 W/mK, 6.45×10^{-12} m^2 and 50%, respectively, for all the simulations in this section. The other material properties and boundary conditions are taken to be the same as in Table I and Table II; the TIMs and TC Cu block are not included in the simulations here. The condenser side boundary conditions are applied on the lower wall of the TGP device. Two values of ambient temperature, 293 K and 333 K, are investigated to observe its effect on the device performance. Since the convective heat transfer coefficient on the condenser side is prescribed to be very high (8240 W/m^{2}K), the ambient temperature is essentially realized on the condenser side of the vapor chamber. The simulation results reveal the vapor core to be an important design parameter for optimizing the performance of the vapor chamber at the lower ambient temperature condition (293 K). The other input parameters to be optimized for given desired outputs are then discussed, followed by the optimization analysis for these ultra-thin TGPs.

1) TGP thermal resistance and pressure drop

Fig. 12(a) shows the TGP resistance, the vapor core thermal resistance as well as the total and vapor flow pressure drops for various heat flux inputs for the 1 mm thick nominal TGP and the condenser-side ambient temperature of 293 K. It is interesting

to note that the thermal resistance of the 1 mm thick TGP decreases as the input heat flux is increased from 18 to 89 W/cm^2, in contrast to the behavior of the 3 mm thick TGP where the thermal resistance was noted to be constant over this range of heat flux. The thermal resistance of the vapor core is found to be significant (~40% of R_{TGP}) in the case of this thinner vapor chamber, unlike the case of the 3 mm thick device. At smaller length scales, the pressure drop in the vapor core becomes significant due to the high vapor phase velocities (ranging from 15-60 m/s for heat inputs of 18-89 W/cm^2). The high flow pressure drop leads to a significant temperature drop in the vapor core. With increasing heat input, the vapor pressure and temperature drops also increase. However, the thermal resistance of the vapor core decreases as the input heat flux is increased, indicating that the vapor phase pressure and temperature drops do not increase linearly with device heat input. The vapor core saturation temperature increases from 293.4 K to 295.2 K as the input heat flux is increased from 18 to 89 W/cm^2 which also leads to an increase (~20%) in the vapor phase density with input heat flux. Hence, the vapor core flow velocity and correspondingly the vapor core pressure drop do not increase linearly with the device heat input. Fig. 12(a) also shows that the vapor pressure drop accounts for ~25% of the total flow pressure drop for any input heat flux for this ultra-thin vapor chamber, with a 0.25 mm vapor core; similar results were reported by Vadakkan *et al.* [23]. The thermal performance of such a thin vapor chamber device at the prescribed ambient temperature of 293 K is worse than a solid heat spreader made of the substrate material (CuMoCu) which offers a thermal resistance of 0.27 K/W at any heat input. The use of very thin vapor chambers for electronics thermal management for lower ambient temperatures (< 298 K) is only recommended relative to a solid heat spreader if the vapor core resistance in the vapor chamber is decreased. The vapor core resistance may be decreased by increasing its thickness, as discussed in the next section, or by increasing the operating saturation temperature.

When the ultra-thin TGP device operates at a higher condenser side ambient temperature of 60 ºC, however, the vapor core pressure and temperature drops are noted to be insignificant (Fig. 12(b)) as compared to the total pressure drop and TGP total resistance, respectively. At higher condenser temperature, which is also reflected as a higher vapor core saturation temperature, the vapor density increases, leading to a smaller vapor phase velocity which in turn causes smaller flow pressure and temperature drops. Thus, the vapor core thickness is an insignificant design parameter for device applications at higher saturation temperatures, i.e., under conditions at which the chip operates in higher ambient temperature conditions (higher temperature on the condenser side). At the higher operating temperature, predictions from the 1-D and numerical models are in good agreement as the vapor core thermal resistance is low.

Fig. 13(a) and (b) show the temperature contours on the exterior boundaries of the TGP (a one-eighth model is simulated, exploiting symmetry in the device) and the wick-vapor interfaces, respectively, for an input heat flux of 89 W/cm^2 and a condenser side ambient temperature of 293 K. Steep temperature gradients in the transverse direction occur not only in the substrate wall and the wick but also in the vapor core of the device, again in contrast to the thicker TGPs. These simulations

reveal the thickness of the vapor core to be an important parameter for device optimization for low ambient temperature applications.

The resistances of various components of the ultra-thin TGP are computed based on the 1-D resistance network model (Fig. 5(a)) and are presented in Table IV. The resistance network model predicts the TGP resistance to be 0.26 K/W. However, the numerical model predicts the TGP resistance to be in the range of 0.51-0.56 K/W at the lower heat flux inputs. The reason for this under-prediction of the TGP resistance by the resistance network model is the inappropriate accounting of the vapor core resistance. It is clear that simplified resistance network models presented in the literature [15] are not adequate for predicting the performance of very thin vapor chambers, and that the resistance of the vapor core should be appropriately factored into the computations.

2) TGP design parameters and performance optimization

The variable parameters in the TGP device are: substrate wall thickness; thickness, porosity and pore radius of the wick structure; thickness of the vapor core; and size and location of the porous posts and of the evaporator (heat-input region). The output (performance) parameters are the thermal resistance and the capillary limit (or the maximum heat transport capability) of the device. The different input parameters affect the two outputs in different ways and to different extents. For example, an increase in the thickness of the wick structure leads to an increase in the thermal resistance. At the same time, generally, the heat transport capability of the device also increases with increasing wick thickness since the liquid flow pressure drop is reduced due to the greater cross-sectional area available for flow. However, as noted above, a greatly reduced vapor core thickness resulting from an increase in wick thickness beyond a certain extent leads to increased flow pressure drop in the vapor core and adversely affects the heat transport capability at small vapor core saturation temperatures.

Changes in the vapor chamber performance in response to variations in the wick and vapor core thicknesses is explored for a 1 mm thick TGP with a fixed substrate wall thickness of 0.25 mm and the condenser side ambient temperature of 293 K. The cases considered in this optimization study are summarized in Table V. The wick thickness is varied from 0.05 mm to 0.25 mm, with a corresponding variation of vapor core thickness from 0.4 mm to 0.2 mm. In all four cases, a 0.05 mm thick wick is included on the condenser side of the TGP. The boundary conditions utilized for the optimization study are also presented in Table V. The wick thermal conductivity, permeability and porosity are taken as 30 W/mK, 6.45×10^{-12} m^2 and 50%, respectively.

Fig. 14(a) shows the variation of the TGP thermal resistance with wick thickness and input heat flux for a condenser-side ambient temperature of 293 K. The vapor chamber thermal resistance is very sensitive to wick thickness at any input heat flux, and is highest for the largest wick thickness (0.25 mm). The TGP resistance also decreases with an increase in the input heat flux. It is less sensitive to the input heat flux for small wick thicknesses while it decreases significantly with the increase in input heat flux when the wick thickness is large and the vapor core is very thin. This is because the vapor core thermal resistance is

significant at small core thicknesses and it decreases with increasing heat flux, thus decreasing the overall TGP resistance. Fig. 14(b) shows the response surface for the total flow pressure drop in the TGP device, presented for different wick thicknesses (thus varying vapor core thicknesses) and heat flux inputs. At low heat inputs, the total pressure drop is relatively insensitive to wick thickness. However, its variation is significant at larger heat fluxes (~100 W/cm^2). The total pressure drop decreases as the wick thickness is increased (from 0.05 mm to 0.2 mm), while it increases marginally due to an increase in the vapor pressure drop as the wick thickness increases from 0.2 to 0.25 mm.

As discussed above, a trade-off in the variation of the TGP resistance and flow pressure drop (which determines the heat transport capability of the vapor chamber) as the wick thickness is varied from 0.05 mm to 0.25 mm. To achieve the optimum wick thickness that minimizes both the thermal resistance and the flow pressure drop, a cost function (CF) is formalized as shown below:

$$\begin{aligned} CF &= w_1 R_{TGP}\big|_{norm} + w_2 \Delta P_{total}\big|_{norm} \\ R_{TGP}\big|_{norm} &= \frac{R_{TGP}}{R_{TGP}\big|_{\max}}, \Delta P_{total}\big|_{norm} = \frac{\Delta P_{total}}{\Delta P_{total}\big|_{\max}} \end{aligned} \tag{17}$$

In eq. (17), the cost function is derived from the normalized TGP thermal resistance and total flow pressure drop, assigning different weights to the two output parameters. In the present analysis, equal weights (w_1, w_2 = 0.5) are assigned to the two outputs. The objective in the optimization is to minimize the cost function *CF*. The resulting variation in *CF* with changes in the wick thickness and the input heat flux is shown in Fig. 15. It is noted that for applications with small heat flux inputs, the smallest wick thickness (= 0.05 mm) is optimal for the device performance. For applications with greater heat loads, however, a moderate wick thickness of 0.1 mm leads to the minimum cost function and thus optimum performance.

VI. Summary and Conclusions

In the present work, a three-dimensional numerical model has been developed to predict the performance of two-phase heat spreaders such as heat pipes and vapor chambers using water as the working fluid. The model is used to simulate the performance of a 3 mm thick vapor chamber, also referred as a Thermal Ground Plane (TGP). The model is validated by performing experiments on custom-fabricated TGPs. It is noted that the vapor chamber performs as a better heat spreader than a solid block only at higher heat fluxes (> 100 W/cm^2) for the given geometry and mounting surface temperature. At these heat fluxes, nucleate boiling occurs in the wick structure, leading to a decrease in its thermal resistance. The vapor chambers are fabricated with porous posts for mechanical integrity of the device under sub-atmospheric operating pressures. The porous posts lead to a shorter path for liquid return from the condenser to the evaporator regions of the device, thus decreasing the liquid flow

pressure drop in the wick structure. The model and experiments show that the vapor chamber works as an excellent heat spreader at high heat flux inputs (> 100 W/cm^2).

The model is also employed to optimize the performance of a 1 mm thick TGP device. At this thickness and a vapor core saturation temperature of 293 K, the vapor core poses a significant thermal resistance and the vapor pressure drop is comparable in magnitude to the liquid pressure drop in the wick. However, at a higher condenser-side ambient temperature of 333 K, which also leads to a higher saturation temperature in the vapor core of the device, the vapor pressure drop and thermal resistance are noted to be negligible. The simulations reveal that the vapor chamber thermal resistance at low saturation temperatures does not scale with its thickness when the vapor core resistance starts to become significant. An optimum wick thickness that minimizes both the flow pressure drop and the device thermal resistance is identified based on an optimization study. Over the range of wick thicknesses (0.05-0.25 mm) chosen in the present study, the smallest wick thickness of 0.05 mm and a moderate wick thickness of 0.1 mm are noted to maximize the thermal and hydrodynamic performance of the ultra-thin vapor chambers at low and high heat flux inputs, respectively.

REFERENCES

[1] M. Lu, L. Mok, and R. J. Bezama, "A Graphite Foams Based Vapor Chamber for Chip Heat Spreading," *Journal of Electronic Packaging*, vol. 128, pp. 427, 2006.

[2] I. Sauciuc, G. Chrysler, R. Mahajan, and R. Prasher, "Spreading in the Heat Sink Base: Phase Change Systems or Solid Metals?," *IEEE Transactions on Components and Packaging Technologies*, vol. 25 (4), pp. 621-628, 2002.

[3] S. Kalahasti, and Y. K. Joshi, "Performance Characterization of a Novel Flat Plate Micro Heat Pipe Spreader," *IEEE Transactions on Components and Packaging Technologies*, vol. 25 (4), pp. 554-560, 2002.

[4] Y. F. Maydanik, S. V. Vershinin, M. A. Korukov, and J. M. Ochterbeck, "Miniature Loop Heat Pipes – A Promising Means for Cooling Electronics," *IEEE Transactions on Components and Packaging Technologies*, vol. 28 (2), pp. 290-296, 2005.

[5] J. Legierski, and B. Wiecek, "Steady State Analysis of Cooling Electronic Circuits Using Heat Pipes," *IEEE Transactions on Components and Packaging Technologies*, vol. 24 (4), pp. 549-553, 2001.

[6] R. Ranjan, J. Y. Murthy, and S. V. Garimella, "Analysis of the Wicking and Thin-film Evaporation Characteristics of Wick Microstructures," *ASME Journal of Heat Transfer*, vol. 131, pp. 101001 (1-11), 2009.

[7] R. Ranjan, J. Y. Murthy, and S. V. Garimella, "A Microscale Model for Thin-film Evaporation in Capillary Wick Structures," *International Journal of Heat and Mass Transfer*, vol. 54 (1-3), pp. 169-179, 2011.

[8] R. Ranjan, J. Y. Murthy, S. V. Garimella, and U. Vadakkan, "A Numerical Model for Transport in Flat Heat Pipes Considering Wick Microstructure Effects," *International Journal of Heat and Mass Transfer*, vol. 54 (1-3), pp. 153-168, 2011.

[9] R. Ranjan, J. Y. Murthy, S. V. Garimella, and U. Vadakkan, "A Numerical Model for Transport in Heat Pipes Considering Wick Microstructure Effects," *12th IEEE Intersociety Conference on Thermal and Thermomechanical Phenomena in Electronic Systems (Itherm)*, 2-5 June 2010, Las Vegas, NV, 2010.

[10] U. Vadakkan, S. V. Garimella, and J. Y. Murthy, "Transport in Flat Heat Pipes at High Fluxes from Multiple Discrete Sources," *ASME Journal of Heat Transfer*, vol. 126, pp. 347-354, 2004.

[11] U. Vadakkan, J. Y. Murthy, and S. V. Garimella, "Transient Analysis of Flat Heat Pipes," *Procs. ASME Summer Heat Transfer Conference*, July 21-23, Las Vegas, Nevada, 2003.

[12] K. H. Do, S. J. Kim, and S. V. Garimella, "A Mathematical Model for Analyzing the Thermal Characteristics of a Flat Micro Heat Pipe with a Grooved Wick," *International Journal of Heat and Mass Transfer*, vol. 51 (19-20), pp. 4637-4650, 2008.

[13] G. Carbajal, C. B. Sobhan, G. P. Peterson, D. T. Queheillalt, and H. N. G. Wadley, "A Quasi-3D Analysis of the Thermal Performance of a Flat Heat Pipe," *International Journal of Heat and Mass Transfer*, vol. 50, pp. 4286-4296, 2007.

[14] Y. Koito, H. Imura, M. Mochizuki, Y. Saito, and S. Torii, "Numerical Analysis and Experimental Verification on Thermal Fluid Phenomena in a Vapor Chamber," *Applied Thermal Engineering*, vol. 26, pp. 1669-1676, 2006.

[15] R. Prasher, "A Simplified Conduction Based Modeling Scheme for Design Sensitivity Study of Thermal Solution Utilizing Heat Pipe and Vapor Chamber Technology," *ASME Journal of Electronic Packaging*, vol. 125, pp. 378-385, 2003.

[16] J. A. Weibel, S. V. Garimella, and M. T. North, "Characterization of Evaporation and Boiling from Sintered Powder Wicks fed by Capillary Action," *International Journal of Heat and Mass Transfer*, vol. 53 (19-20), pp. 4204-4215, 2010.

[17] D. H. Altman, J. R. Wasniewski, M. T. North, S. S. Kim, and T. S. Fisher, "Development of Micro/nano Engineered Wick-Based Passive Heat Spreaders for Thermal Management of High Power Electronic Devices," *Proceedings of the ASME 2011 InterPACK*, Portland, OR, July 6-8, 2011, InterPACK2011-521122, 2011.

[18] N. J. Gernert, J. Toth, and J. Hartenstine, "100 W/cm^2 and Higher Heat Flux Dissipation Using Heat Pipes," *13th International Heat Pipe Conference (13th IHPC)*, Shanghai, China, September 21-25, 2004.

[19] R. W. Schrage, 1953, *A Theoretical Study of Interface Mass Transfer*, New York: Columbia University Press.

[20] V. P. Carey, *Liquid-Vapor Phase Change Phenomena*, Hemisphere Publishing Corp., Washington DC.

[21] W. Rose, "Interphase Matter Transfer, the Condensation Coefficient and Dropwise Condensation," *Proc. 11th Int. Heat Transfer Conf.*, Kyongju, Korea, vol. 1, pp. 89-104, 1998.

[22] Fluent Inc., 2004, FLUENT 6.2 User's Guide.

[23] U. Vadakkan, S. V. Garimella, and J. Y. Murthy, "Prediction of Dryout in Flat Heat Pipes at High Heat Fluxes From Multiple Discrete Sources" *ASME International Mechanical Engineering Congress and Exposition*, November 15–21, 2003, Washington, DC, USA, paper no. IMECE2003-42444, pp. 741-751, 2003.

Ram Ranjan is a Senior Research Scientist at United Technologies Research Center. He received his Ph.D. in mechanical engineering from Purdue University in 2011. In his current role, Dr. Ranjan is responsible for the ongoing development of thermoelectric-based Active Cooling Modules (ACM) for DoD systems and projects related to thermal management issues in UTC products. He has four years of experience in the field of electronics thermal management and development of CFD tools for various engineering applications and his areas of expertise include vapor chamber heat spreaders, porous media and phase-change heat transfer (evaporation, boiling) in nanostructure coated surfaces. Prior to joining UTRC, Dr. Ranjan worked as a Research Assistant at Purdue University for four years on projects related to thermal management of high power electronics. He is also a member of ASME and IEEE and has published his research findings in over 16 publications, including 7 peer-reviewed articles in international conferences.

Jayathi Y. Murthy is Robert V. Adams Professor of Mechanical Engineering at Purdue University and Director of PRISM: NNSA Center for Prediction of Reliability, Integrity and Survivability of Microsystems,. She received her Ph.D degree from the University of Minnesota in the area of numerical heat transfer and has worked in both academia and in industry. During her employment at Fluent Inc., a leading vendor of CFD software, she developed the unstructured solution-adaptive finite volume methods underlying their flagship software Fluent, and the electronics cooling software package ICEPAK. More recently, her research has addressed sub-micron thermal transport, and the development of numerical techniques for concurrent electro-thermal simulation in emerging electronic devices. She is the recipient of the IBM Faculty Partnership award 2003-2005, the 2004 Journal of Electronics Packaging Best Paper award, the 2007 ASABE Best Paper Award, the 2008 ASME HTD Best Paper Award and the 2009 EPPD Woman Engineer of the Year award Prof. Murthy serves on the editorial board of *Numerical Heat Transfer*, is an editor of the 2nd edition of the *Handbook of Numerical Heat Transfer,* and serves as Associate Editor of the ASME *Journal of Heat Transfer.* She has served on numerous national committees and panels on electronics thermal management and CFD, and is the author of over 270 technical publications.

Suresh V. Garimella is the R. Eugene and Susie E. Goodson Distinguished Professor of Mechanical Engineering at Purdue University. He received his PhD from the University of California at Berkeley in 1989. He is Director of the NSF Cooling Technologies Research Center. His research interests include thermal microsystems, energy efficiency in computing and electronics, micro- and nano-scale transport phenomena, electromechanical microfluidic actuation, high-

performance compact cooling technologies, renewable and sustainable energy systems, and materials processing. Dr. Garimella has co-authored over 450 refereed journal and conference publications and 13 patents/patent applications, besides editing or contributing to a number of books.

Dr. Garimella serves as Associate Editor of ASME Thermal Science and Engineering Applications, and as an Editor of Applied Energy, International Journal of Micro and Nanoscale Transport and Experimental Heat Transfer, and has served as Associate Editor of ASME Journal of Heat Transfer and Editor of Heat Transfer-Recent Contents and on the Editorial Board of Experimental Thermal and Fluid Science. He is a Fellow of the ASME. His efforts in research and engineering education have been recognized with the 2010 Heat Transfer Memorial Award; 2009 ASME Allan Kraus Thermal Management Award; 2010 Distinguished Alumnus Award from IIT Madras; 2009 Harvey Rosten Award for Excellence; 2004 ASME Gustus L. Larson Memorial Award; K16 Clock Award from the ASME; 2009 Purdue University Distance Teaching Award; Graduate School/UWM Foundation Research Award, 1995; UWM Distinguished Teaching Award, 1997; and Society of Automotive Engineers' Ralph R. Teetor Educational Award, 1992. Most recently, he was selected as a Jefferson Science Fellow (2010-'11) to provide scientific input to foreign policy issues in the U.S. State Department.

David H. Altman is a Principal Engineer in Raytheon Integrated Defense Systems Advanced Technology Programs Directorate. His work focuses on research and development into thermal management and energy system technologies for next generation defense electronics. His interests include development of advanced device scale, heat spreader, thermal interface, cold plate and cooling system technology incorporating emergent materials and system concepts. David holds BS and MS degrees from Rensselaer Polytechnic Institute and Boston University.

Mark T. North is an Engineering Group Leader at Thermacore, Inc. He received his Ph.D. in mechanical engineering from Cornell University in 1993. At Thermacore, Dr. North is responsible for development of advanced technologies for heat pipes and systems based on heat pipes. His work also includes advanced single phase cooling for air-cooled heat sinks, as well as advanced applications for heat pipes. Dr. North has co-authored over 40 technical publications, holds 6 US patents, and is currently serving as an Associate Editor for the Journal of Thermal Science and Engineering Applications.

Tables and Figures

Table I

THERMOPHYSICAL PROPERTIES OF MATERIALS IN THE VAPOR CHAMBER

Substrate wall (CuMoCu)	Thermal conductivity Specific heat Density	167.8 W/m K 285 J/kg K 9890 kg/m^3
Solid Property of Wick (Cu)	Thermal conductivity Specific heat Density	59.4-79.4 W/m K 381 J/kg K 8978 kg/m^3
Water	Thermal conductivity Specific heat Density Viscosity	0.6 W/m K 4182 J/kg K 1000 kg/m^3 8×10^{-4} N s/m^2
Water vapor	Thermal conductivity Specific heat Density Viscosity	0.026 W/m K 2014 J/kg K 0.01 kg/m^3 8.49×10^{-3} N s/m^2
Water/vapor	Latent heat of vaporization	2446.36 kJ/kg

Table II

THERMOPHYSICAL MATERIAL PROPERTIES AND BOUNDARY CONDITIONS USED IN THE MODEL

Component in the Model	**Property/Boundary Condition**	**Value**
5000S35 0.02’’ BQ pads (TIM) (R = 1 K cm^2/W)	k_{TIM} t_{TIM}	0.5 W/m K 0.05 mm
TC Cu block	k_{Cu}	387.6 W/m K
Evaporator	Heat flux	18-477 W/cm^2
Condenser	h_{amb} T_{amb}	8240 W/m^2 K 293 K

Table III

VALUES OF VARIOUS RESISTANCES (K/W) IN THE 1-D NETWORK MODEL FOR THE 3 MM THICK TGP

R_{TGP1}	R_{TGP2}	R_{TGP3}	R_{TGP4}	R_{TGP5}	R_{TGP6}	R_{TGP7}
0.85	4×10^{-2}	1.1×10^{-3}	~0	1.1×10^{-3}	7.4×10^{-3}	3.4×10^{-3}

Table IV

VALUES OF VARIOUS RESISTANCES (K/W) IN THE 1-D NETWORK MODEL FOR THE 1 MM THICK TGP

R_{TGP1}	R_{TGP2}	R_{TGP3}	R_{TGP4}	R_{TGP5}	R_{TGP6}	R_{TGP7}	R_{TGP}
0.25	7.2×10^{-3}	1.11×10^{-3}	~0	1.1×10^{-3}	3.77×10^{-3}	1.66×10^{-3}	0.26

Table V

WICK AND VAPOR CORE THICKNESSES AND BOUNDARY CONDITIONS USED FOR THE OPTIMIZATION STUDY OF 1 MM THICK TGP DEVICE

Geometric Parameters		
	Thickness (mm)	
	Wick	Vapor Core
	0.05	0.4
	0.1	0.35
‘Nominal’ Case	0.2	0.25
	0.25	0.2
Boundary Conditions		
Evaporator	Heat flux	18-89 W/cm^2
Condenser	h_{amb} T_{amb}	8240 $W/m^2 K$ 293 K

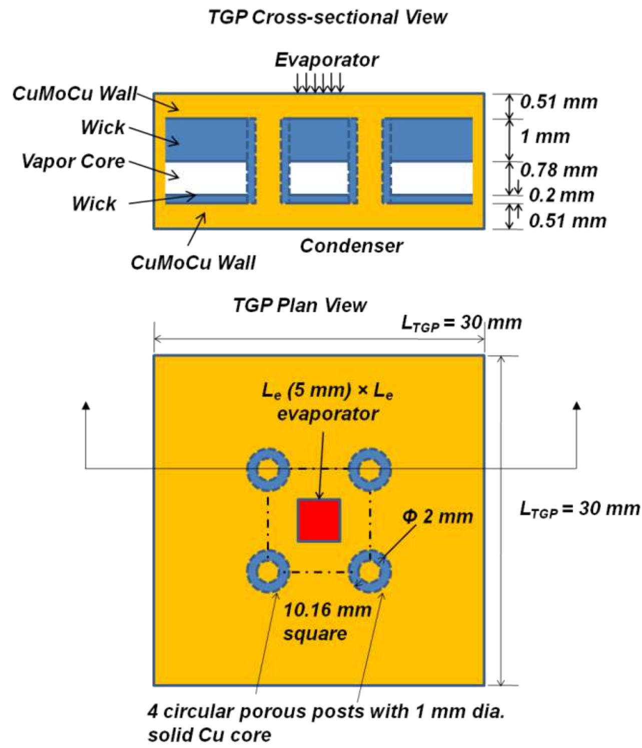

Fig. 1. Side and plan views of the thermal ground plane device (TGP) showing the substrate, wick and vapor regions including porous posts.

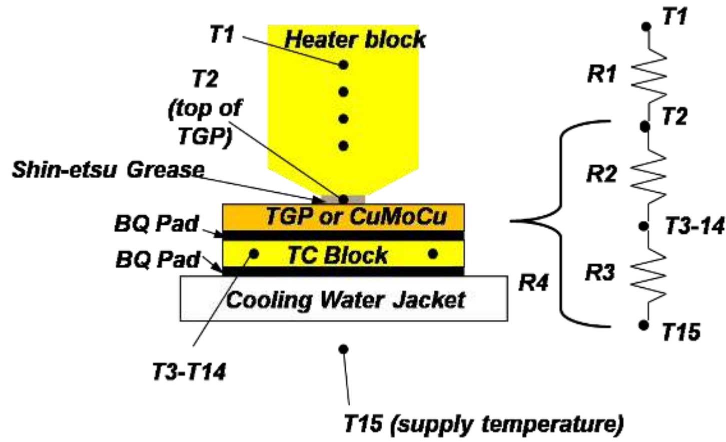

Fig. 2. Test setup showing various parts and locations of the temperature measurements and the corresponding thermal resistance network.

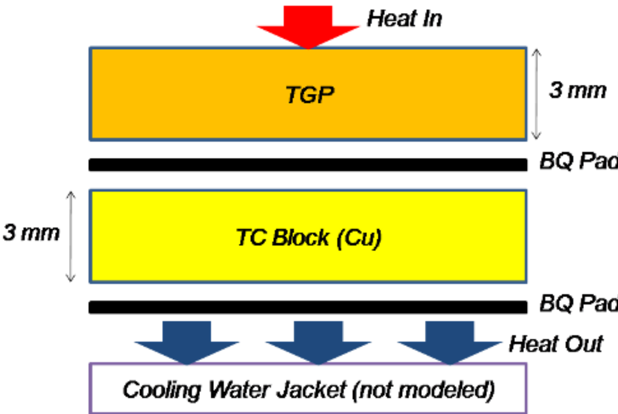

Fig. 3. Schematic diagram of the experimental setup showing various blocks represented in the model.

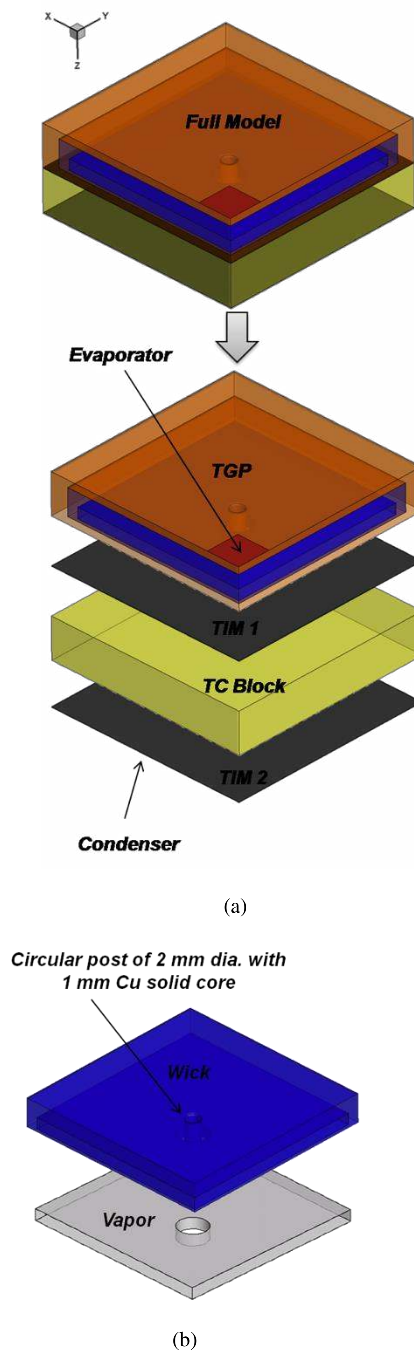

Fig. 4. (a) Computational domain showing the various parts modeled, and (b) wick and vapor domains in the TGP, depicting the porous post structure.

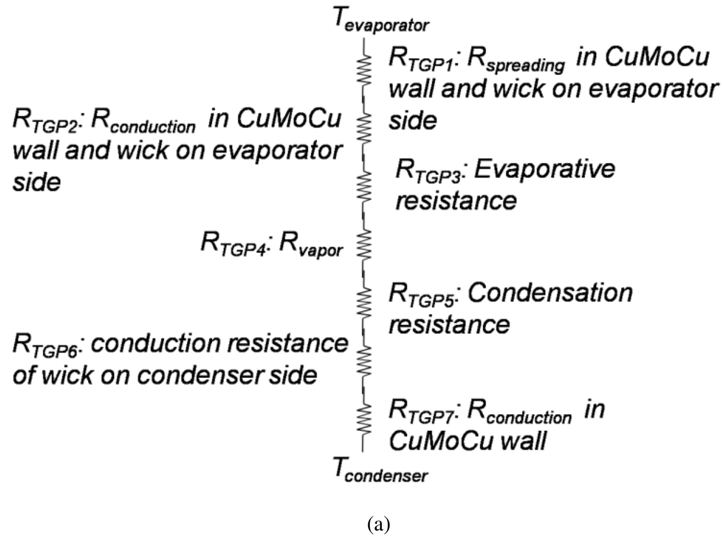

(a)

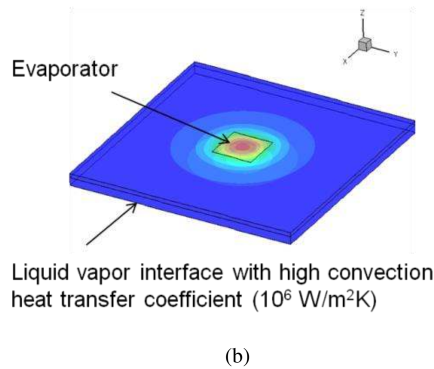

(b)

Fig. 5. (a) One-dimensional thermal resistance network of the TGP, and (b) temperature contours in the substrate and wick domains for computation of spreading resistance.

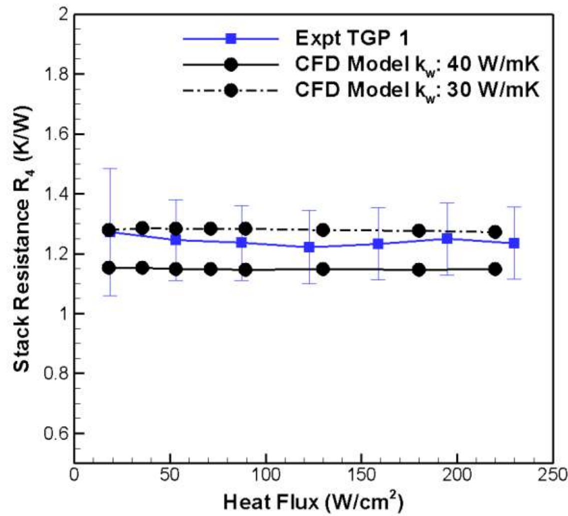

Fig. 6. Comparison of stack resistance (from TGP center to coolant) predicted by the CFD model with experimental measurements for theTGP device with a 200 µm thick wick on condenser side.

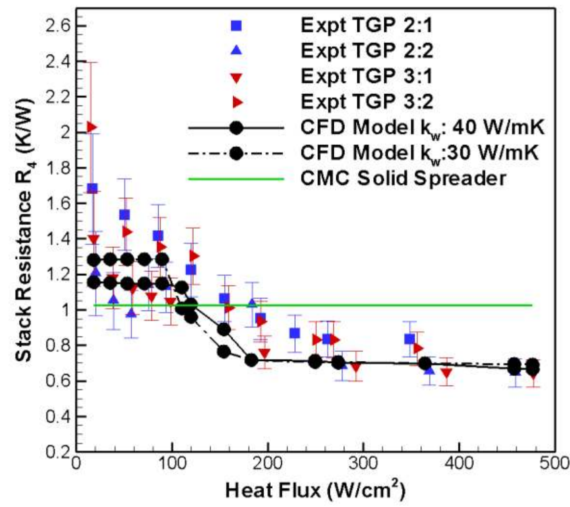

Fig. 7. Comparison of stack resistance from the CFD model with experimental values for TGP devices with no wick on the condenser side.

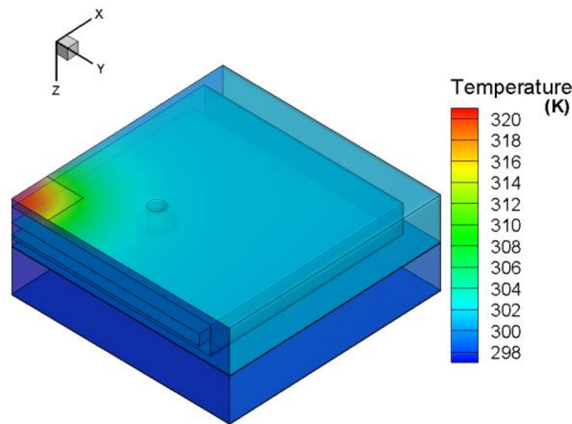

Fig. 8. Temperature contours on the outer surfaces of the computational model for evaporator heat flux of 89 W/cm^2.

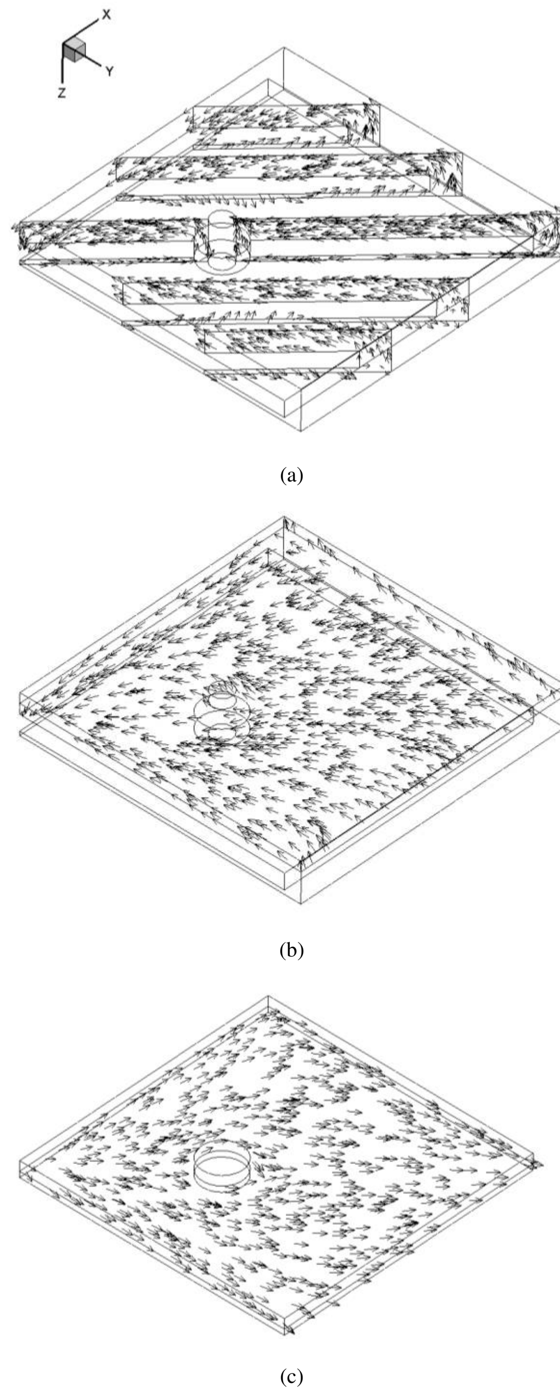

Fig. 9. Flow vectors in (a) different vertical planes of the wick structure depicting feeding flow from condenser to evaporator regions through the porous post; (b) a horizontal plane of the wick structure on evaporator side; and (c) a horizontal plane in the vapor space.

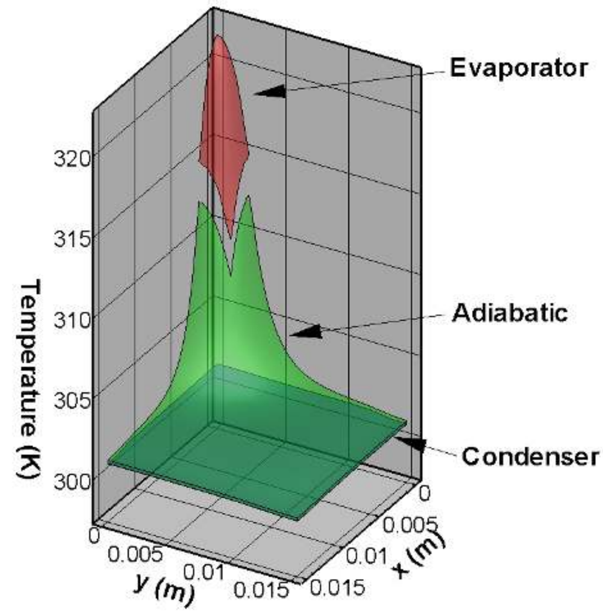

(a)

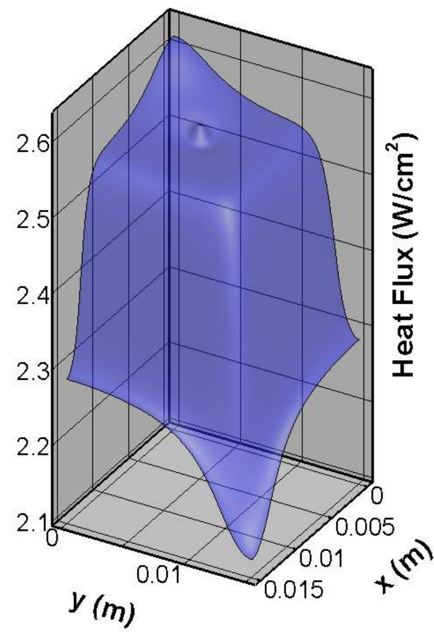

(b)

Fig. 10. (a) Temperature, and (b) heat flux on the outer walls of the TGP for an evaporator heat flux of 89 W/cm^2.

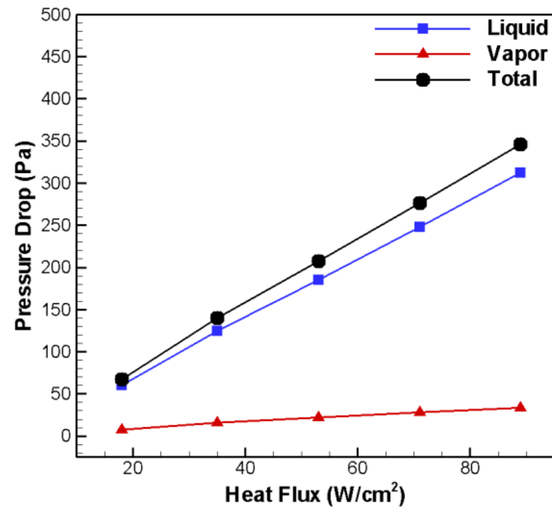

Fig. 11. Flow pressure drops in the TGP at different evaporator heat flux and an operating temperature of 293 K.

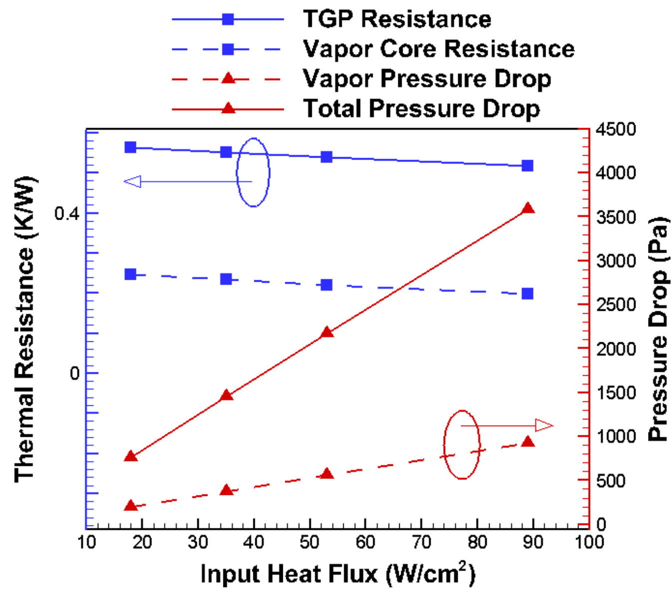

(a)

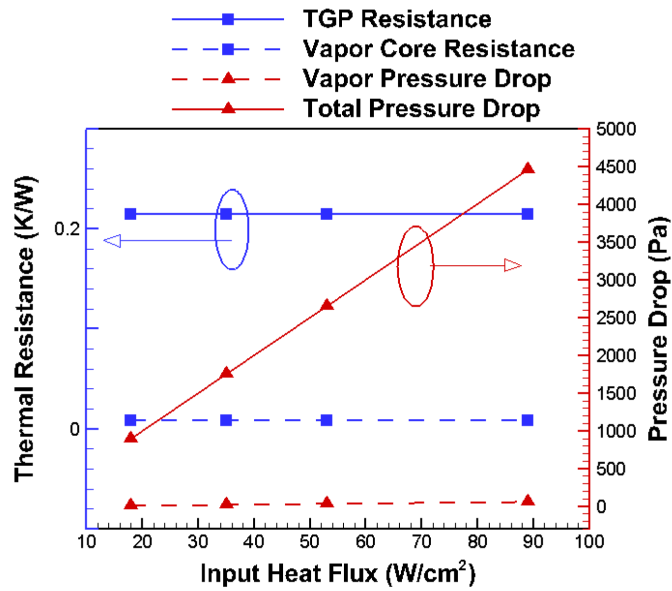

(b)

Fig. 12. Thermal resistance, vapor and liquid pressure drops in the TGP vs input heat flux for a condenser-side ambient temperature of (a) 293 K, and (b) 333 K.

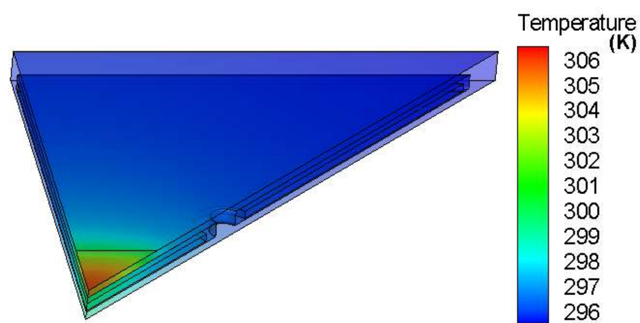

(a)

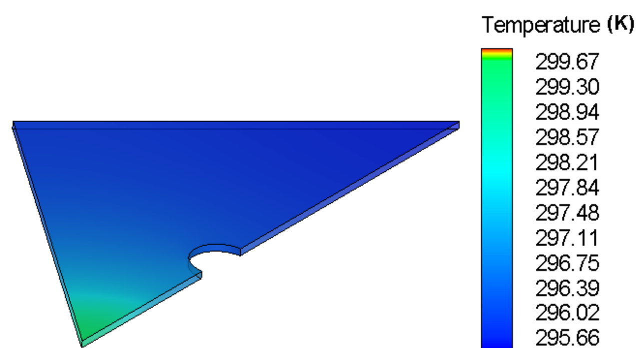

(b)

Fig. 13. Temperature contours on (a) the external boundaries of the nominal TGP device (with 0.25 mm wall, 0.2 mm wick and 0.25 mm thick vapor core), and (b) at the boundaries of the vapor core for input heat flux of 89 W/cm^2 and a condenser-side ambient temperature of 293 K.

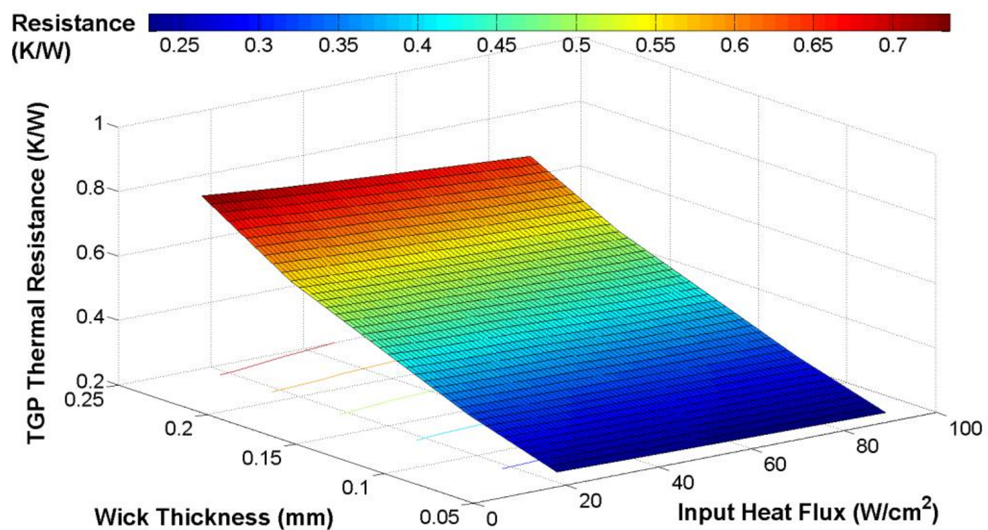

(a)

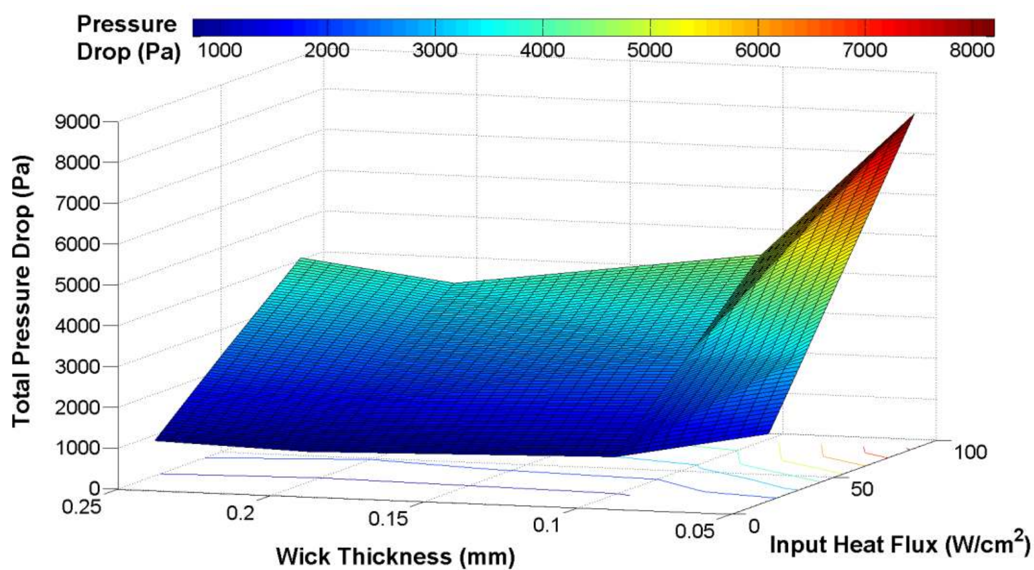

(b)

Fig. 14. (a) TGP thermal resistance, and (b) total flow pressure drop for various wick thickness values in the 1 mm thick TGP at different heat fluxes for the condenser side ambient temperature of 293 K.

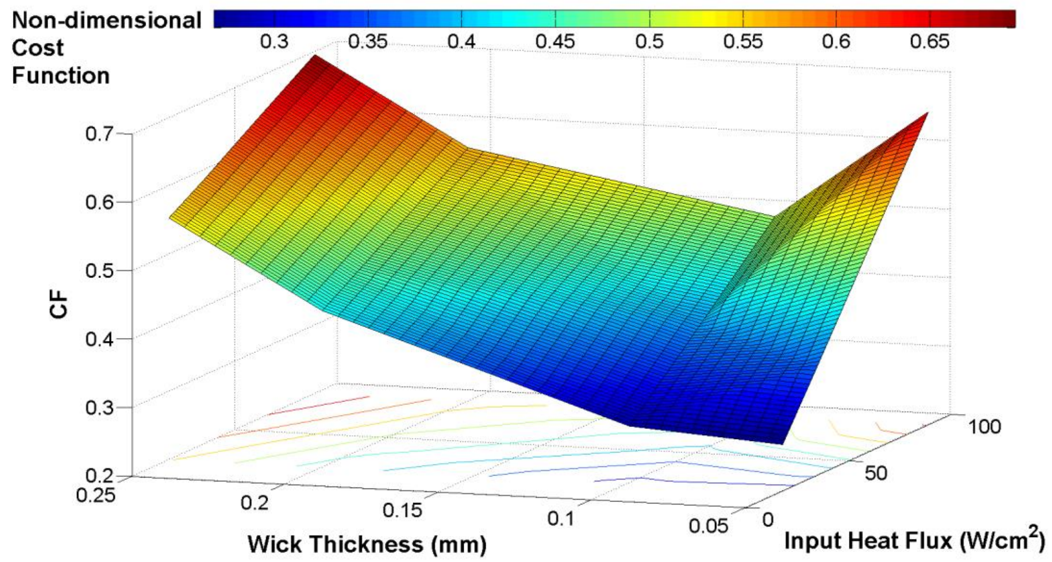

Fig. 15. Cost optimization function with equal weights assigned to the TGP resistance and flow pressure drops plotted for various wick thicknesses and input heat flux values.